

A Compliant Rolling Ellipsoidal Thumb Joint for the TU Hand

Spenser Pulleyking^{ID}, Graduate Student Member, IEEE, and Joshua Schultz^{ID}, Senior Member, IEEE

Abstract—This work presents a compliant rolling ellipsoidal carpometacarpal (CMC) joint for the thumb of a robotic hand. This work is the first to introduce the biellipsoidal joint, a flexure hinge-based biomimetic thumb CMC joint. A model of this design is implemented in simulation and in experiment and compares the manipulability metrics, a quality metric for the end-effectors within robotic manipulators, across similar workspaces. Compliant mechanisms known as flexure hinges maintain the 3-D rolling of the ellipsoids rather than sliding or slipping. By comparing the results for the biellipsoidal joint with a gimbal joint, the relative size and location of the region of highest manipulability were found to be similar between CMC joint models, although the shape of this region varied somewhat from one to the other. The experimental comparison used tendon-displacement data generated from bio-inspired hardware prototypes of both the biellipsoidal CMC joint and gimbal CMC joint models for two similar robotic thumbs, whereas the analytical version used iterative forward kinematics to derive and compare the manipulability metric distributions.

Index Terms—Biomimetic and bio-inspired robotics, grasping and manipulation, robotics.

I. INTRODUCTION

THE usefulness of biological hands emerges subtly from underlying relationships in a compliant network of rigid and soft bodies, tendons, and ligaments. Thumb use exploits this while controlling our own hand, but research is still exploring how simplified inputs can model complex grasping tasks [1]. In our design of a robotic thumb, we seek to explore a compliant network comprised of tendons, bearings, and flexure hinges: a heterogeneous thumb-like structure [2].

Actuated grasping, which conforms to the shape of the object shows promise and this may contribute to the inverse correlation between any given tool's ubiquity and prevalence in human tasks, and the number of its degrees of freedom (DoF) [3], [4].

Manuscript received 2 March 2023; revised 28 July 2023; accepted 21 September 2023. Recommended by Technical Editor W. J. Chris Zhang and Senior Editor G. Berselli. This work was supported by the NSF under Grant 1427250. (Corresponding authors: Spenser Pulleyking; Joshua Schultz.)

The authors are with the Department of Mechanical Engineering, University of Tulsa, Tulsa, OK 74104 USA (e-mail: spenser-pulleyking@utulsa.edu; joshua-schultz@utulsa.edu).

This article has supplementary material provided by the authors and color versions of one or more figures available at <https://doi.org/10.1109/TMECH.2023.3324185>.

Digital Object Identifier 10.1109/TMECH.2023.3324185

Take for instance the screwdriver and the scalpel, although both are rigid objects, the couplings between the DoF of a system are differently affected when a closed loop is formed by a grasped object. The screwdriver configures itself in a functional human grasp to have 2-DoF (linear or rotary motion about its centerline), whereas a scalpel can be used in all six possible DoFs. In addition to grasping devices, haptic feedback devices also model the conformation between a human hand and the device, and such close-loop kinematics are again of benefit to consider [5]. The contribution of this article is a design, functional prototype, analysis, and characterization of a CMC joint where the flexion-extension and abduction-adduction axes are colocated, and an evaluation of the effects on the manipulability of this design choice from the perspective of the tendon displacements. This design brings the added benefits of the resistance to compressive loads and the passive restoring force of the rolling magnetic ellipsoids, while flexure hinges restrain the motion so that the joint only exhibits the motions seen in the human thumb. The flexure hinge design prevents sliding and pivoting motions that cause loss of the grasped object.

Starting from the palm, the anatomical joints of the thumb are commonly referred to as the carpometacarpal (CMC), the metacarpophalangeal (MCP), and the interphalangeal (IP) joints. Treating the IP joint as mobile, the MCP joint as fixed, and the CMC joint as rolling without gliding or slipping, the device is implemented in The University of Tulsa Anthropomorphic Robotic Hand, or the TU Hand [6], [7], [8]. Biological joints' connective tissue limits shearing motions between contact surfaces: there is a strong preference for minimizing slipping during rolling, which may also allow for more precise kinematic motions [9]. It is not uncommon for devices whose axes of motion are unfixed to have both rolling and/or sliding motions, constructed to maintain only what rolling or sliding is desired [10]. Due to the CMC joint's high level of interpersonal variability, there is also significant disagreement on a discrete assignment of the location and orientation of the axes of revolution or translation [11]. This region, sometimes known as the trapezio-metacarpal complex, consists of interactions between eight bones and 12 ligaments. There is no straightforward way to implement such a complex model using a traditional kinematic pair [12].

Using a gimbal (perpendicular joint with intersecting axes) in robotic hands appears to be one of the most common CMC joint 2-DoF configuration. A list of anthropomorphic robotic hands with gimbal thumb CMC joints includes the *AllegroHand*, *ShadowHand*, and *iCub* biomimetic robotic hands [13], [14], [15].

The notion of a gimbal is based on a pair of orthogonal Dof and is often at the core of the state-of-the-art thumb CMC joint design. While these thumbs may not be considered to be biologically inspired, their design may benefit from the symmetry in the sensors of their similar opposing digits, which precludes the need to design an independent thumb model [16], [17]. In addition to recent commercially available myoelectric prostheses, arthrodesis (joint fixation at a specific pose) is also being used to take advantage of simplified design to preserve functionality [18]. As in prior work, the MCP joint is treated as fixed to reduce complexity [6]. To the best of the authors' knowledge, no research has yet explored the influence of arthrodesis on manipulability. Robotic hand systems with fewer inputs than outputs are simpler to control than full-actuated equivalent systems [19].

Hybrid soft-rigid robotic grippers conform to objects during manipulation, without complex planning of each phalanx's position and orientation [20], [21]. To measure the ability of a digit, such as grasping or in-hand object manipulation, the manipulability metric (MM) quantifies the ability of an end effector to be moved smoothly in any direction in the workspace [22]. Many uses of the MM exist: one extension is the dynamic MM, which can be used to evaluate dynamic grasping [23]. Our system of the tendon-driven thumb is designed to reduce complexity without substantially reducing function, taking inspiration from the biological TM complex. Prior to this article, this work was partially published only to develop the simplified manipulability metric (SMM), a quick approximation of the MM [7].

The rest of this article is organized as follows. In Section II, a compliant mechanism is presented to constrain the internal components of two rolling ellipsoids that constitute a 2-DoF thumb CMC joint. In Section III, the application of this metric to a tendon-driven system is established, and two Jacobians are computed to inform the MMs of our tendon-driven and joint-angle systems. In Section IV, the prototype hardware is described as it pertains to this experiment. In Section V, kinematic models for both our rolling ellipsoidal CMC joint and a gimbal CMC joint are presented. In Section V-A, the Denavit–Hartenberg (DH) parameters for the models are developed and discussed. In Section VI, the data collection and procedure are described for gathering the end-effector and tendon displacement data throughout the experimental workspace. In Section VII, the MMs are calculated, and in Section VIII the results of the analytical and simulated experiments are discussed. Finally, Section IX concludes this article.

II. COMPLIANT FLEXURE HINGES TO CONSTRAIN ROLLING ELLIPSOIDS

Flexure Hinges provide a unique function to devices known as hard–soft robotic hands [21]. By customizing the geometry of the device's biomimetic components, such as in the case of this article with the surfaces of the ellipsoids, the design can more closely match its biological inspiration. The biellipsoidal joint, as long as all other coupled geometric parameters are also changed when the ellipsoids' parameters change, can be built from any two similar prolate ellipsoids, with some variation. The ellipsoid geometry chosen for the physical experiments is one

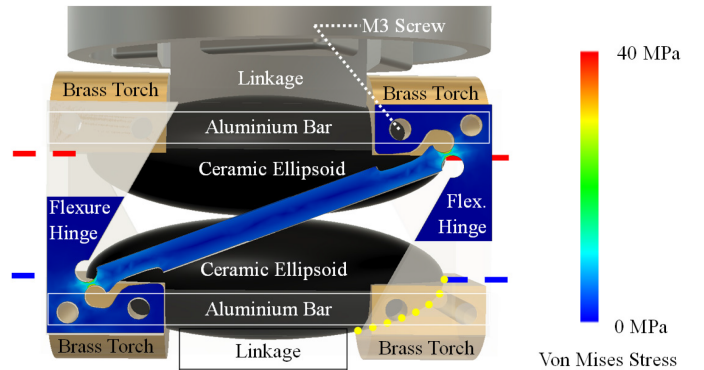


Fig. 1. Close-up image of a CAD model for the biellipsoidal joint, which highlights the Von-Mises stresses in one of the flexure hinges.

of cost-efficiency, as the ceramic magnets needed are readily and cheaply available. When two ellipsoids are in contact, to constrain constant lengths between the opposing foci is challenging, as sliding may occur at the contact point. We present a pair of compliant mechanisms with flexure hinges to join the foci such that both abduction–adduction and flexion–extension motion can occur. Because the structural integrity of the joint relies on a series of consistent centers of rotation relative to the ellipsoids, two flexure hinges are developed to meet that specification: as each flexure hinge localizes its motion about at least two points, both the front and rear flexure hinge of the CMC joint can each be considered distributed-type compliant mechanisms [21], [24].

Rolling mechanisms need constraints to ensure proper contact between the surfaces, if not, the device may still tolerate some degree of slippage but must be able to at least closely approximate rolling without slipping for intentional motion [25]. This means that the rolling motion for abduction–adduction can occur within the ellipsoids' carriage, but the foci are held a fixed distance apart at all poses as described by Blake [26], “each focus of the one remains at a constant distance, viz. the transverse axis of one of the ellipses, from a focus of the other.” The flexure hinges also provide a restoring force that will center the joint when unloaded. Polypropylene was selected for the hinges' material. A finite element analysis was performed on the final flexure hinge design, which confirmed that the flexure hinge was within the bounds of elastic deformation for the given material, as shown in Fig. 1. The C-type hinges are shown to have stress concentrations and may host some deformation, but the geometry tolerates it while restricting the overall motion.

In tandem with the flexure hinges, four brass “torches” were created to house the ends of the ellipsoids: together, this sub-assembly forms a “carriage” for the motion of the ellipsoids. As the torches are linked to the flexure hinges with screws, the prolate ends of the ellipsoids within the torches are constrained, so that the ellipsoids cannot exit the torches, as shown in Fig. 1. The torches are linked to the flexure hinges and are linked by thin aluminum crossbars: together, the constraints imposed fully define the position of both ellipsoids. The brass torches' inner profile is highlighted on one of the four torches with a dotted

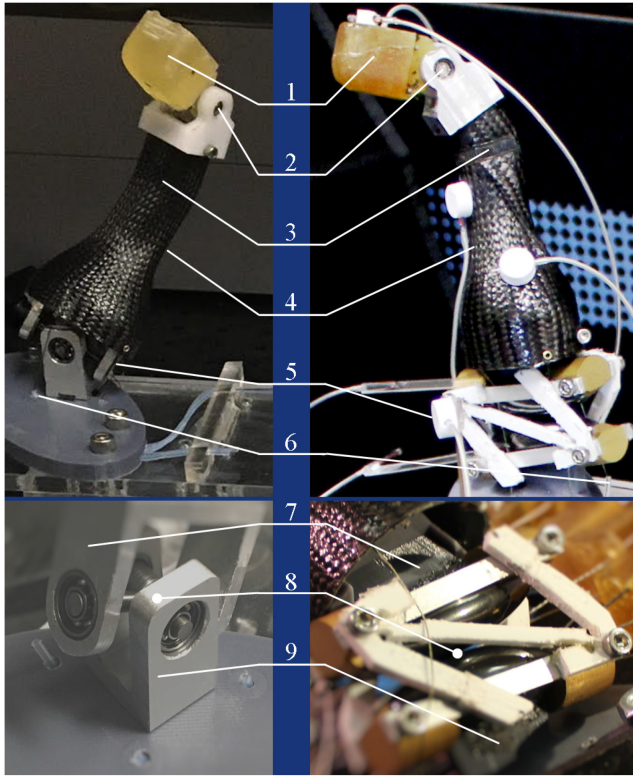


Fig. 2. Comparison of similar features between the two thumb prototypes. Their intentional difference is the nature of the CMC joint architecture, with the traditional gimbal CMC joint shown on the left-hand side, and the biellipsoidal CMC joint introduced in this article on the right-hand side. 1. Distal phalanx. 2. Pin joint: MCP fusion to distal phalanx. 3. Point of joint fixation of MCP fusion. 4. Carbon fiber skin of MCP fusion. 5. CMC joint 6. Teflon-tube nylon-tendon entry sheath. 7. CMC upper phalanx (part of MCP fusion) 8. Point of intersection of CMC axes of motion. 9. CMC lower phalanx (part of thumb base).

yellow line in Fig. 1. The lower base ellipsoid is embedded below the surface of the palm, and the upper ellipsoid is embedded in the metacarpal bone of the thumb, so the contact surface will consist of only a subregion of one semiellipsoid of each, as shown in Figs. 1 and 2.

III. MANIPULABILITY OF TENDON-DRIVEN END-EFFECTORS

$$MM = \sqrt{\det(J(\theta)J(\theta)^T)}. \quad (1)$$

A set of four MM distributions are calculated as follows.

- 1) Tendon manipulability (ellipsoidal).
- 2) Tendon manipulability (gimbal).
- 3) Standard (joint-task space) manipulability (ellipsoidal).
- 4) Standard (joint-task space) manipulability (gimbal).

Standard forward kinematics predict the joint angles' correspondence with the end-effector's position, while also measuring tendon displacement. Each path will produce a distinct version of the Jacobian to consider when calculating an MM for our thumb: the joint space to task space matrix, and the tendon excursion to task space matrix. This is due to the use of a tendon-drive mechanism with inextensible tendons. The

TABLE I
ANGLE MEASUREMENTS ARE SHOWN IN DEGREES

Structure	Variable	Length (mm)
Metacarpal	ℓ_{mcp}	74.63
Proximal phalanx	ℓ_{pp}	27.88
Distal phalanx	ℓ_{dp}	34.26
DoF	Variable	Range of motion (deg)
CMC joint flexion/extension	μ	$0^\circ \leftrightarrow 70^\circ$
CMC joint abduction/adduction	σ	$-20^\circ \leftrightarrow 20^\circ$
IP joint flexion/extension	ω	$-15^\circ \leftrightarrow 80^\circ$

Jacobian derived from joint space and the Jacobian derived from tendon excursion will each be generated and discussed, in the context of both experimental verification with a physical prototype, and with a computer simulation using a symbolically-generated dataset based on the forward kinematics of both CMC joint prototypes. The fact that the MCP is a fixed joint, in both the model of the joint angles and the physical prototype, is inspired by surgical arthrodesis [6], [7]. As the MCP joint is fixed in both cases, the MM will be compared between the rolling CMC joint introduced here and the gimbal CMC joint, and the benefits of the two designs will be considered.

The Jacobian matrix functions as a mapping between the joint-angle velocities and the velocity of the end effector, but it can be applied to quantities other than the joint space variables, such as tendon excursions. Our prototypes demonstrate that a Jacobian and corresponding MM derived from tendon-displacement inputs in place of joint angle information will produce similarly useful results. The tendon-based Jacobian used to calculate the MM for our two physical prototypes, J_A , is shown in (2), and the traditional joint-based Jacobian used to calculate the MM for our two analytical simulations, J_T , is shown in (3): as it uses joint angles, the variables are the same as those used in Table I.

$$J_A = \begin{bmatrix} \frac{\delta x}{\delta d_1} & \frac{\delta x}{\delta d_2} & \frac{\delta x}{\delta d_3} & \frac{\delta x}{\delta d_4} \\ \frac{\delta y}{\delta d_1} & \frac{\delta y}{\delta d_2} & \frac{\delta y}{\delta d_3} & \frac{\delta y}{\delta d_4} \\ \frac{\delta z}{\delta d_1} & \frac{\delta z}{\delta d_2} & \frac{\delta z}{\delta d_3} & \frac{\delta z}{\delta d_4} \end{bmatrix} \quad (2)$$

$$J_T = \begin{bmatrix} \frac{\delta y}{\delta \mu} & \frac{\delta y}{\delta \sigma} & \frac{\delta y}{\delta \omega} \\ \frac{\delta z}{\delta \mu} & \frac{\delta z}{\delta \sigma} & \frac{\delta z}{\delta \omega} \end{bmatrix}. \quad (3)$$

For the tendon-based Jacobian matrix in (2), there are two independent columns: one for coupled flexion/extension of the CMC joint and IP joint, and one for the abduction/adduction of the CMC joint. As we introduce this “tendon-Jacobian” J_T , it should be contrasted with the standard Jacobian. The tendon-Jacobian was evaluated by sampling the experimental data, whereas the standard Jacobian was generated by sampling the kinematic model. From a tendon networking perspective, by the application of Caratheodory’s theorem, four actuators are sufficient to fully actuate three joints, given certain tendon configurations, and assuming that each tendon needs one actuator to pull it separately [27]. Alternatively, each of the four tendons of our three-joint prototypes is designed to share with another tendon, thus, for four tendons, only two sources are required [28]. By configuring two pairs of opposing tendons, one pair being flexion/extension and the other adduction/abduction,

one point of actuation can simultaneously pull two tendons in opposite directions. The fixture of the MCP joint dictates the remaining DoF, as given in Table I.

IV. MECHANICAL DESIGN

The biellipsoidal joint hardware developed for the experimental section can be seen installed on the *TU Hand*, a research platform for similar experimental hardware [29], [30]. Many variants of similar rolling congruent parametric surfaces can be found in various industrial applications and designs, such as elliptical gear/diaphragm meshes, or the mathematical relationship between such general surfaces is well established [26]. An in situ view of this assembly and of a gimbal CMC joint can be seen in Fig. 2. The gimbal CMC is constructed from u-channel brackets with press-fit bearings and two orthogonal pin joints that support the two perpendicular shafts, which are fixed together at their intersection.

The ellipsoids in our biellipsoidal prototype are low-cost pseudoellipsoidal ceramic magnets. These are known as the “Rattlesnake Eggs” toy, and embody ellipsoidal surface contact patches. As outlined in Section II, the ellipsoids’ carriage is manufactured from aluminum, brass, and polypropylene. To best understand how such a network of couplings can be realized in hardware, compare the geometric diagrams, as shown in Fig. 3(a) and (b). The cross-linkages, represented by segments BC and AD, are chosen to enforce a constant distance between the crossed foci of the biellipsoidal joint, as shown in Fig. 3(b). We cannot put a pivot through each focus, as the ellipsoid needs to roll about its major axis in the flexion–extension direction. The solution is that the ellipsoids are able to abduct and adduct, as shown in Fig. 4(b), as well as roll about their major axes, and thus constrain the motion imparted by the four tendons traversing the joint such that the device has a biomimetic range of motion. In Fig. 2, a rigid link termed the MCP fusion is comprised of the metacarpal fused to the proximal phalanx at the angles of the Steiger arthrodesis: 15° flexion and 10° pronation (adduction) [6]. Thin-walled carbon fiber layup was precisely molded to the desired angle of arthrodesis at the MCP joint using an internal 3-D printed scaffold upon which to mold the fiber’s geometry as the resin cures. To do this, a woven carbon fiber sleeve that narrows as it is stretched was held with a weight to conform to the 3-D printed geometry.

The brass and aluminum components, respectively, labeled the “torch” and crossbar, are rigidly coupled together with M3 screws to cage the ellipsoids as they roll and contact the inner torch-shape surfaces, without obstructing their linkage, which extends outside the cage: thus, the boundaries of this rigid body become the mechanical stops of the joint, as shown in Fig. 1. The top and bottom ellipsoid cages are also coupled by two flexure hinges, whose white polypropylene surfaces can be seen around the CMC joint in Fig. 2. These two C-type flexure hinges are to enforce necessary kinetostatic linkage, acting together as a composite compliant mechanism [24]. They were milled out from a $\frac{1}{8}$ sheet of standard grade polypropylene on a *HAAS Mini Mill*. After a few iterations of milling, a desirable geometry

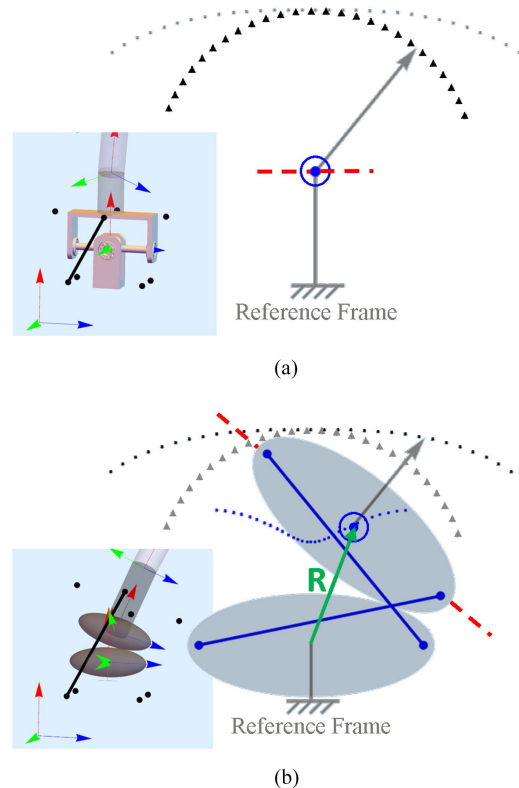


Fig. 3. Kinematic joint diagrams: the trace of the current joint workspace is shown as an array of gray points, with their contrasting joint workspace shown as an array of black points. The CAD drawings align the diagrams with the prototypes; only the flexion tendon is shown, as a black line segment. (a) Gimbal joint with two axes of motion, intersecting and orthogonal. The blue normal vector coming out of the page represents abduction/adduction, while the red dashed vector represents flexion/extension. (b) Bi-ellipsoidal CMC joint is also shown, with blue segments showing the rigid distances between the foci that the flexure hinges maintain, and a curved blue array showing the new internal workspace of the joint. R is defined in (17). (a) Gimbal joint diagram. (b) Biellipsoidal joint diagram.

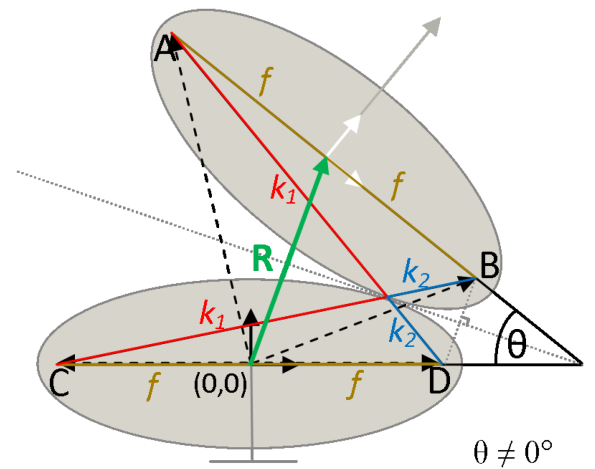


Fig. 4. Biellipsoidal joint’s inner kinematic formulation. Points A, B, C, and D correspond to vectors a , b , c , and d , which are shown as dashed vectors that terminate at the foci of the ellipses. The ellipses represent any possible cross-section between rolling ellipsoids, similarly aligned. The functions for parameters f , θ , k_1 , k_2 , and R are described by (4) through (17).

was found, which was significantly robust: after an estimated 600 cycles per hinge, the final geometry chosen was still performing well.

Although some slight elongation deformation was observed, it was not considered significant enough to constitute “necking” of the flexure hinge joint, a modality indicating impending failure of the hinge. The maximum payload of the system is affected by the flexure hinges, but the most limiting factor in the system as it is measured today is the break strength of the tendons used, which is 18 kg. While grasps will normally involve sharing a load over multiple tendons and points of contact with the hand, this value is a rational estimate for a wide range of commonly grasped objects.

V. KINEMATIC MODEL

The idea of two congruent ellipses (or elliptical cross-sections of 3-D objects) rolling without slipping along a shared tangent, itself coupled to a static length between the opposing ellipses’ foçī, is more than a century old, but it has not seen any major mechanical applications [26], [31]. To define such a system geometrically, a congruent four-bar linkage is shown in Fig. 4. This linkage is a specific case of a “hinge antiparallelogram” joint, which has seen ample research, and can be used to optimize various robotic and mechatronic tasks that are particularly suited to this specific linkage configuration [32].

We will consider a permutation of the four-bar linkage formed by two ellipses whose foçī are rigidly cross-linked as in Fig. 4. This four-bar linkage will share identical kinematics with the rolling ellipsoids, but the ellipsoids provide a contact surface through which forces could be transmitted, such as the loading force on the thumbs and wrists, while lifting a heavy object. Fig. 3 shows a 1-DoF biellipse joint and its resulting workspace. Consider the projection on the plane \mathcal{P} containing the centers of the ellipsoids and the contact point. Modeled as two similar surfaces, the rolling of one ellipsoid over one another allows the abduction–adduction and flexion–extension motions to be collocated as they are in the human CMC joint: abduction–adduction occurs within plane \mathcal{P} , and an additional DoF is introduced for flexure extension, shown in Fig. 3 with a dashed red line.

The bielliptical joint maintains that the all four foçī are joined by two rigid linkages, which exist only between the opposing foçī of each other’s ellipse, as shown by the blue line segments in Fig. 3(b). The contact between the two rigid surfaces also allows them to resist high compressive loadings exceeding those that would shear off pins of small diameter. The orientation of the ellipses to each other is constrained by these rigid linkages into being only a single DoF, as the ellipses roll without slipping at their contact point. Referring to the 2-D system in Fig. 4, the single DoF is shown as the variable θ : defined as the angle between the major axes of the ellipses, this is a crucial parameter, as it carries forward into the final design to define the abduction and adduction of the thumb CMC joint. When transitioning from 2-D to 3-D, the bielliptical joint becomes biellipsoidal, and introduces a second DoF orthogonal to the first, defined by the rolling of two ellipsoids rather than ellipses about one of their prolate axes. This second axis of motion is shown in red in

Figs. 1 and 3. As the brass torches shown in Fig. 1 are constrained to rotate about their respective ellipsoid’s major axis, the upper ellipsoid is constrained to roll about its own major axis, shown in red. The lower ellipsoid is fixed to the palm, it cannot rotate about its own major axis, shown in blue, however, the lower two brass torches can rotate about this blue axis.

All of the following definitions are shown as respective to the geometric relationships outlined in Fig. 4. Only two radii are needed to fully define the dimensions of the minimal 2-D case of our biellipsoidal joint: the similar ellipsoids’ major and minor radii, represented by r_{major} and r_{minor} . The distance from each prolate-ellipsoid’s centroid to either of its foçī is defined as f . The constant distance enforced by the flexure hinges’ internal linkages, defined as the line segments AD and BC, is defined as k . To explain the relationship outlined by the following equation, distances k_1 and k_2 are defined as belonging to the variable-length subsegments created by the crossing of line segments AD and BC

$$k_1 + k_2 = 2 \cdot r_{\text{major}} \quad (4)$$

$$k = k_1 + k_2 \quad (5)$$

$$(2r_{\text{minor}})^2 + (2f)^2 = k^2. \quad (6)$$

Once we have incorporated both major and minor radii definitions into the general form of an ellipse, the center to focus distance, f , is defined as shown in Fig. 4. A neutral position of abduction/adduction corresponds to $\theta = 0$. The coordinate equation defining an ellipse is shown in (4) [33]. The constant length k is defined in (5). Equation (6) is produced as a result of the Pythagorean theorem about the right-triangle BDC. Rearranging (6) in (7), the constant length f is defined in (8)

$$4f^2 = 4r_{\text{major}}^2 - 4r_{\text{minor}}^2 \quad (7)$$

$$f = \sqrt{r_{\text{major}}^2 - r_{\text{minor}}^2}. \quad (8)$$

In the following equations, four internal angles are defined using the points shown in Fig. 4; as these angles are all coupled to the motion of the joint, θ

$$\angle BDC = \frac{\pi + \theta}{2} \quad (9)$$

$$\angle ADB = \arcsin\left(\frac{2f \sin \angle BDC}{k}\right) \quad (10)$$

$$\angle ADC = \angle BDC - \angle ADB \quad (11)$$

$$\angle BCD = \pi - \angle BDC - \angle ADB. \quad (12)$$

Once all necessary angles have been defined, the parametric equations to describe the vectors that locate the foçī of both ellipses, \mathbf{a} , \mathbf{b} , \mathbf{c} , and \mathbf{d} , appear in the following equations:

$$\mathbf{a} = \begin{bmatrix} f - k \cos \angle ADC \\ k \sin \angle ADC \end{bmatrix} \quad (13)$$

$$\mathbf{b} = \begin{bmatrix} -f + k \cos \angle BCD \\ k \sin \angle BCD \end{bmatrix} \quad (14)$$

TABLE II
DENAVIT-HARTENBERG (DH) PARAMETERS FOR TRANSFORMATION
MATRICES M_i

α_{i-1} (deg.)	a_{i-1} (mm)	d_i (mm)	θ_i (deg.)
Rot. x_{i-1} axis	Tran. x_{i-1} axis	Tran. z_i axis	Rot. z_i axis
-90°	0	0	$\mu/2^\circ$
90°	0	0	$90^\circ + \sigma/2^\circ$
-90°	0	R	0°
90°	0	0	$-90^\circ + \sigma/2^\circ$
-90°	ℓ_{mep}	0	$\mu/2^\circ$
90°	0	0	10°
-90°	ℓ_{pp}	0	15°
0°	0	0	ω°
0°	ℓ_{dp}	0	0°

Angle measurements are shown in degrees.

$$\mathbf{c} = \begin{bmatrix} -f \\ 0 \end{bmatrix} \quad (15)$$

$$\mathbf{d} = \begin{bmatrix} f \\ 0 \end{bmatrix}. \quad (16)$$

Vectors \mathbf{a} and \mathbf{b} are the position vectors of points \mathbf{A} and \mathbf{B} , as shown in Fig. 4, in the frame shown in black whose origin is at the center of the stationary ellipse. It could be useful in certain cases to continue the kinematic chain and simply define vector \mathbf{a} or \mathbf{b} as the next linkage of the robot, we define the origin of the next forward kinematic frame as occurring at the center of the mobile ellipse, as shown in white in Fig. 4

$$\mathbf{R} = \begin{bmatrix} \mathbf{a}_x, \mathbf{b}_x \\ \mathbf{a}_y, \mathbf{b}_y \end{bmatrix} \quad (17)$$

where vector \mathbf{R} is the vector between ellipses' centers, as well as in the 3-D model between the ellipsoids centroids; in both cases, it functions as an intermediate frame, which splits the angular motion at the CMC joint between itself and the previous frame, which is located at (0,0) in Fig. 4. This vector is shown in green in both Figs. 3 and 4. Vector \mathbf{R} is defined as the mean of vectors \mathbf{a} and \mathbf{b} , as shown in (17), and it also defines the motion of the center point of the upper ellipse. The kinematic modeling of the gimbal joint is outlined in Table II. Both the gimbal and the biellipsoidal models' abduction/adduction tendons terminate past the CMC joint. Their flexion/extension tendons continue further, and thus are coupled with motion at both the CMC joint and the IP joint, terminating near the fingertip on the distal phalanx (DP).

A. Comparison Via DH Parameters

It should be noted that for both the planar and spatial cases of identical spheres (but not for identical ellipsoids), a rolling without-sliding relationship has been effectively demonstrated in a prototype robotic wrist and elbow joint [34], [35]. Drawing from this idea, our design and prototypes represent the first design considered that allows the generalization of the joint surface geometries from spheres to ellipsoids. This primarily allows our model to tune the major and minor radii to select the best available geometry of the ellipse for any given joint.

By bringing the rolling-ellipse relationship in 2-D into any possible pose's cross-section in 3-D, an ellipsoidal relationship can similarly be built, which incorporates rolling over the surface. This solves the challenge of colocated joints: by having two ellipsoids roll over one another, the location is shared without compromising the resistance to compressive reaction forces. For example, reaction forces, which would impart a shear load on the gimbal joint's pins would be better managed by the biellipsoidal joint, which distributes the contact force into the palm. The DH parameters of the thumb with the ellipsoidal rolling CMC joint and a gimbal CMC joint are outlined in Table II. A virtual prismatic joint is used to represent the translation of the center of the moving ellipse as it rolls without slipping. Interestingly, these DH parameters can represent both the gimbal CMC joint and the biellipsoidal CMC joint: the gimbal CMC joint is just a special case of the biellipsoidal case, as the gimbal CMC joint is the case where \mathbf{R} goes to zero. Looking at the kinematics outlined by the DH parameters in Table II, the biellipsoidal parameters are identical to the gimbal parameters, for the case that $\mathbf{R} = 0$: the kinematic models still work for this condition, although they require some extra frames to calculate as compared with the more direct kinematic model for a gimbal joint. Table II depicts variables μ and σ , respectively, representing the motions of flexion/extension and abduction/adduction, which collocate at the CMC joint. Because of the MCP joint's arthrodesis, no motion occurs. Finally, the IP joint is modeled as having a normal range of motion in the DP, as represented by variable ω in Table II.

VI. DATA COLLECTION PROCEDURE

The tip of the thumb was moved throughout its workspace, involving both the IP joint and the 2-DoF CMC joint, and the excursions of the four tendons were recorded. Data were collected at 240 Hz using a *Saleae Logic* signal recorder. The base of the thumb was mounted to the lab bench, with the tendons connected to carriages on linear slides (see Fig. 5) similar to those used in the experiments of Schultz and Rake [30]. The tendons are attached to weighted springs that pass through Teflon tubes that run through the polylactic acid (PLA) lab stand, shown in gray in Fig. 2, before re-entering the MCP Fusion. One carriage is attached to each tendon and moves with it; with the gravitational load on the weights, the carriages follow the movements of the thumb without the tendons ever going slack. The position of the carriages was measured using Avago encoders with U.S. digital encoder strips supplying 158 edges per centimeter. Use of a magnetic orientation sensor, *Polhemus Liberty*, was employed to track the x , y , and z coordinates and orientation of the thumb tip in the base frame through its workspace. The end effector data was in Cartesian space with Euler angles, and the system also reported for each data point a Polhemus sensor quality metric that consistently indicated measurements collected were free from significant distortion. All components that are relevant are shown in Fig. 5. If the tendon path is erroneously interrupted due to collision with an unexpected surface somewhere along its length, it is recorded as a "catch point" in the data.

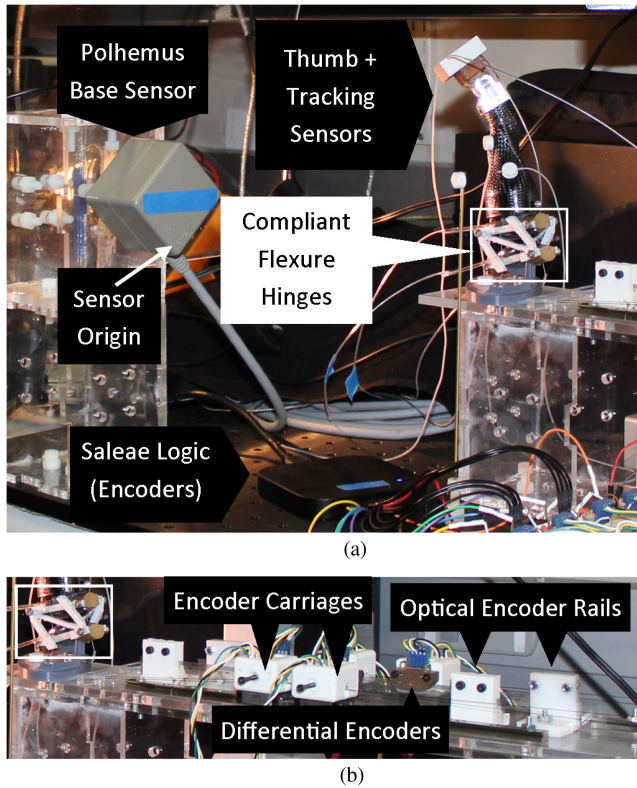


Fig. 5. Experiment setup. (a) Workspace of the robotic thumb, the magnetic wired Polhemus sensors and base sensor, and Saleae logic analyzer. The origin of the base's magnetic field is printed on top of the base (gray box). The sensors remained proximal to the elevated base, such that surrounding objects did not interfere with the sensing. (b) Four white 3-D printed carriages on linear rails, each with a differential optical encoder to track displacement. (a) Prototype experiment workspace. (b) Tendon displacement synchronization.

When finding all possible MMs across all possible poses of the thumb, each pose has a corresponding forward kinematics solution in the task space, upon which the MM value has been superimposed graphically in Figs. 7 and 8. For all four plots, the relative magnitude of these values is represented by the color of each dot at each point cloud.

VII. RESULTS

The MMs were calculated for four cases, as shown in Figs. 7 and 8, with the following results.

- 1) Tendon manipulability (ellipsoidal): **1.0e-3**
- 2) Tendon manipulability (gimbal): **3.1e1**
- 3) Standard manipulability (ellipsoidal): **2.3e-3**
- 4) Standard manipulability (gimbal): **2.5e-3**

A. Joint Space to Task Space MM

For the analytical cases, as shown in Fig. 7, the MM was calculated numerically using finite differences on a grid of points in the workspace, achieved by evaluating the forward kinematics at a grid of points in the joint space. A crescent-shaped subregion of the workspace can be visually identified as having a higher MM than elsewhere in the workspace. Comparing the output graphics

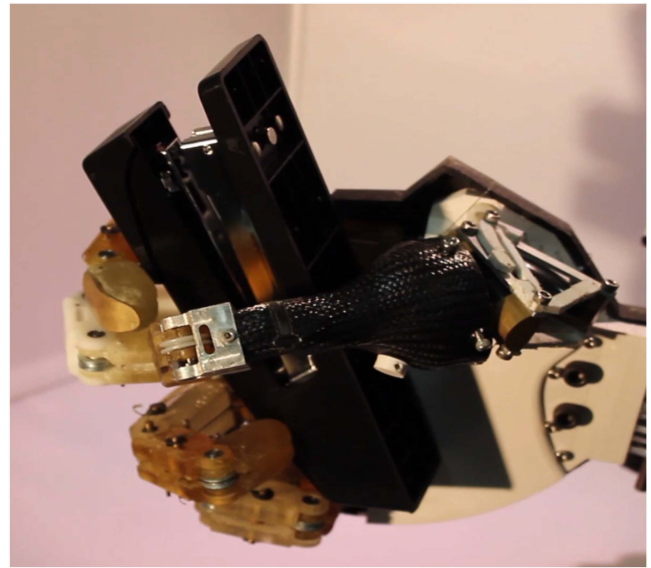


Fig. 6. Biellipsoidal CMC joint and Arthrodesized MCP joint mounted on the TU Hand, shown with the thumb in flexion, while being used in conjunction with the other digits of the hand to grasp a stapler vertically.

of the gimbal CMC joint and the biellipsoidal CMC joint, we see that the volume and size of the high-MM regions are similar, but the shape differs between the two: the region is noticeably wider and more bulbous at the ends of the biellipsoidal CMC joint. In addition, the entire biellipsoidal workspace appears somewhat wider and thinner.

One can also observe from the resulting workspace visualizations of the MM workspace shape that the models are kinematically similar, and while there is no major effect on the magnitude of MM at any given point, the biellipsoidal model does result in a more distributed region of high-MM values. As shown in Fig. 7(b) and (c), the highest density of high-MM values appears to be near the far side of the workspace, just above the metacarpal phalanx of the fourth and fifth fingers. These insets also show that the high-MM values appear to be in an elongated region in the biellipsoidal case, shown in Fig. 3(b), as compared with the traditional (gimbal) hinge-joint case in Fig. 3(a). To the best of the authors' knowledge, there has not yet been a comparable human study of thumb manipulability across the entire workspace. However, anyone may consider this possibility based on the simple observations of one's own thumbs, by observing what thumb positions permit the greatest degree of thumb tip rotations while requiring as little translation as possible.

B. Tendon Extension to Task Space MM

To calculate the tendon-to-task space Jacobian J_T , a cubic grid of approximately 30 000 points $p_i \in W$ was chosen from within the workspace to help localize and aggregate the values of the 120 000 data points collected. The Jacobian was computed from the experimental data at each of these cubic grid points. A linear regression was performed on the experimental data points (each of which had position data in the task space and associated

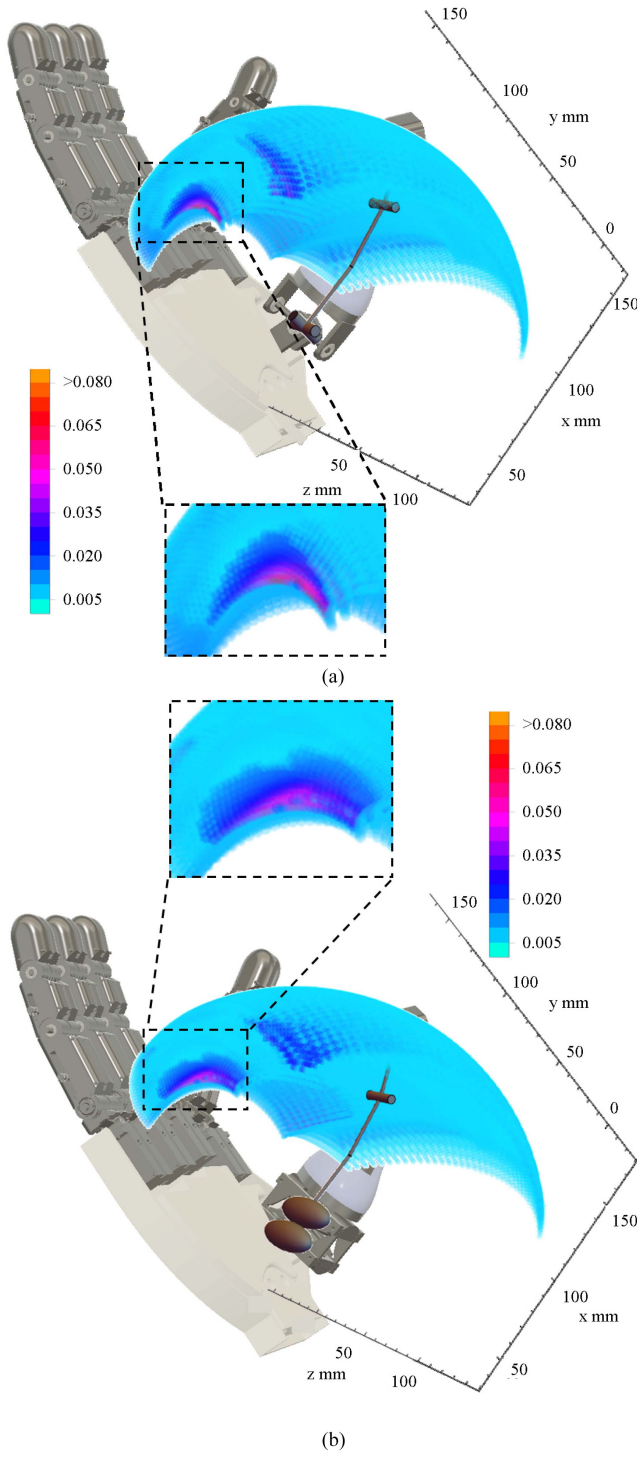


Fig. 7. Joint space to task space MM comparison. The color shows the value of the MM as calculated for all regions of the thumb-tip's workspace. (a) Gimbal CMC—analytical result. (b) Biellipsoidal CMC—analytical result.

tendon excursions) within a neighborhood \mathcal{N} of each p_i . \mathcal{N} consists of all points p_j whose Euclidean distance from p_i is less than a specific threshold: if the points are close enough to one another, the joint angles can only change by a small amount, and J_T is nearly constant over all p_j in \mathcal{N} .

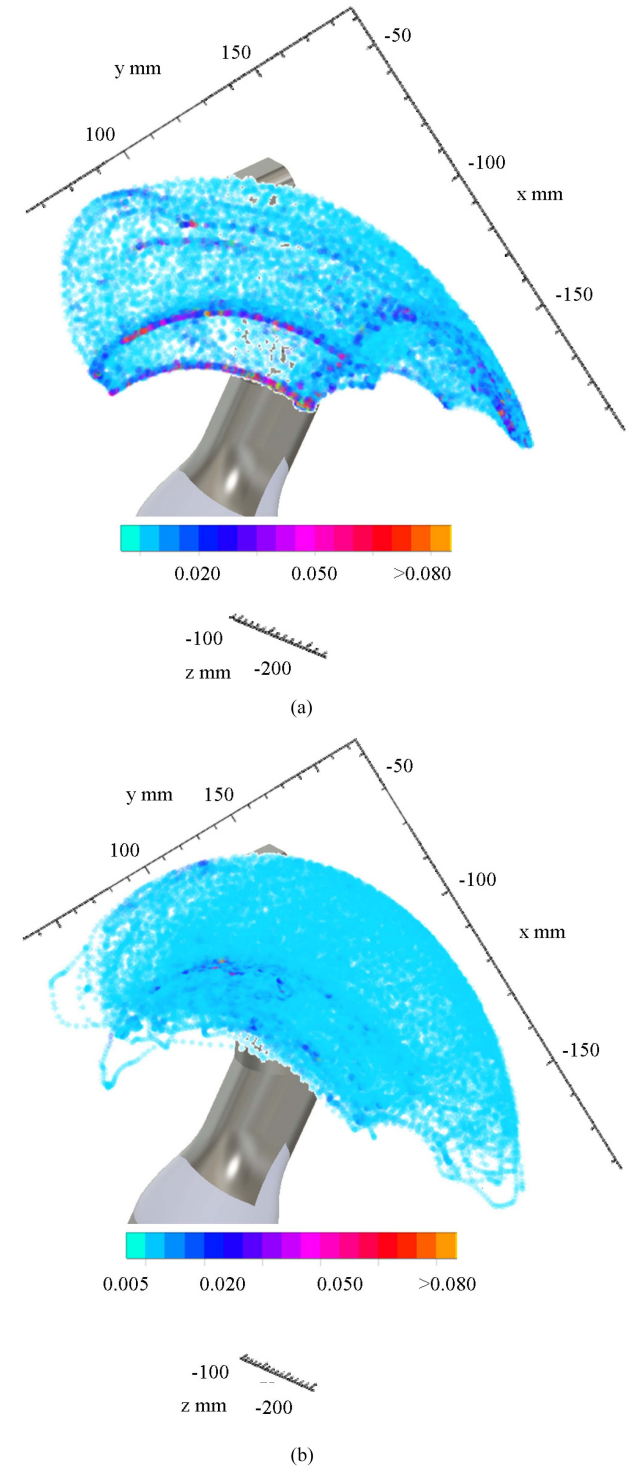


Fig. 8. Tendon excursion to task space MM comparison. The color shows the value of the MM as calculated for all regions of the thumb-tip's workspace. (a) Gimbal CMC—experiment result. (b) Biellipsoidal CMC—experiment result.

From this Jacobian, the MM at each point was calculated across the workspace, from the standpoint of the tendon excursions, rather than from joint angles, and its magnitude is represented by color intensity. The color intensity is uniform over the region, with the exception of the edges of the workspace.

As the mechanical stop simply truncates the nonjoint-limited workspace at an arbitrary boundary, there is no mathematical reason to see high values there. For this reason, any high values are likely due to catch points or bouncing on the encoders as the thumb encounters the mechanical stop. This suggests that from the standpoint of tendon excursions, the MM is more uniform when calculated for tendon displacement than for joint angle displacement.

VIII. DISCUSSION

The experimental plots shown in Fig. 8 and the analytical plots shown in Fig. 7 show the results of calculating the MM for a field of points in the thumb's workspace, and both figures use the same data processing technique. These four workspace color mappings appear to indicate that the tendon excursion to task space MM is somewhat consistent over the workspace, at least within the joint limits considered for a bio-inspired thumb. These joint limits are similar to those in humans, so for a human-like range of motion the manipulability values are low and consistent: this further indicates that no large motions should suddenly result from small tendon excursions in certain locations of the workspace.

The fixated joint at the thumb model's MCP joint restricts the size of the dense central region of high MM values, which is best seen in the two analytical models shown in Fig. 7. If MCP joint motion was allowed, a larger central region of high MM values would likely be observed. However, this does not say for certain that a larger size of the region of high manipulability would inherently be more practically useful, nor justify the additional cost and complexity. The MM data is recorded as a comparison between the proposed biellipsoidal and the traditional design so that the relative merits of the designs can be robustly compared, and this is possible because manipulability can be directly expanded into a family of formal indices known as the manipulability indices [36], [37]. One example of applied manipulability indices is to predict how the kinematics of any thumb-like manipulator influence its ability to navigate a smartphone [38]. However, within all current variations of these indices, there is a tacit assumption that every joint in the manipulator is actuated, whereas this article considers the manipulability when an arthrodesis at the MCP joint is applied.

Despite having a reduced number of DoFs compared with the human hand, as a result of the MCP fixation, our system is analytically predicted to have a central region of the joint space to task space MM values that are around one order of magnitude higher than other regions in the workspace, for both the gimbal CMC joint and biellipsoidal CMC joint prototype cases. The analysis shown in Fig. 7 considered only the joint space kinematics, rather than the tendon space kinematics; subsequently in Fig. 8, the analysis utilized the observed tendon excursions and end-effector positions through time to calculate the task space MM. However, alternative formulations of similar metrics could draw upon the tendon space kinematics. In this work we have only characterized the tendon displacement to thumb tip location experimentally, in principle an analytical model could be created using the methods of Schultz and Rake [30]. Due to the 3-D

nature of the thumb CMC joint, this model would be long and cumbersome to present, and space does not permit us to develop and present it in this work. Furthermore, the density of points in the experimental characterization makes it suitable to be used in look-up table fashion for relating tendon displacements to thumb tip positions in applications, bypassing a need for this model. The tendon displacement function of the CMC is more complex and would not fit the general formula presented in this article, as it is presented. This is because the CMC joint's range of motion is increased, compared with a human range of motion, to counteract the loss of workspace volume from fixating the MCP joint.

Compare this with other regions in the workspace, where large changes in joint angles may result in only slight changes in the task space. It should be noted that the joint-angle Jacobian does not capture any information about the changes in the length of the tendons as the thumb moves due to changing tendon pathway lengths, and so does not represent the inputs and outputs of the system as it is operated in practice: for this, the tendon excursion to task space MM represents a better measure. In either case, a relatively consistent manipulability over the workspace is a benefit, because it reduces the need to move some of the tendons over a large displacement in some regions, while moving very small distances in others, which can be difficult to precisely actuate in operation of the hand during grasping. This central region of high MM values is most apparent in the analytical plots of Fig. 7 and can be seen up close to highlight its geometry: its apparent crescent shape is due to elevated MM values in that region. However, this region does not appear in the plots generated by tendon displacement, suggesting that the relationship between the joint space and the tendons is possibly inverting any region of elevated manipulability. At poses within the high-manipulability region, small changes in joint angles or tendon displacements can thus cause relatively small motions in task space; however, near poses outside this region, small changes in joint angles or tendon displacement may cause larger and undesired motion in task space.

While a gimbal is considered kinematically to consist of two rotational axes meeting at a point, in applications the components of which it is compromised take up physical space, which affects how practical they are in these applications: in practice their range of motion is limited and tendons cannot pass through the gimbal hardware, as shown in Fig. 2. To make the gimbal small, small shafts need to be used, which are in danger of shearing when loads are applied to the thumb. The ellipsoids offer a kinematically more stable tendon-driven thumb: the tendon paths vary with the pose, which makes catch points and tendon collisions difficult to predict. Should the tendons catch on the ellipsoids, the smooth rolling motion distributes the tendons away from potential catch points, while the gimbal does not.

In summary, when compared with the biellipsoidal CMC joint variant, the manipulability of the gimbal CMC joint thumb prototype appears to be of a smaller characteristic high-manipulability region when visualized in the workspace: both in terms of the shape of the region and the elevated values, which comprise the regions themselves, as shown in Figs. 7 and 8. These differences, while visually apparent, are more subtle in

their effect. As presented in Section VII, the MM values differ, but are within an equivalent order of magnitude throughout the entire workspace for all cases considered, except for the tendon-derived gimbal case. This suggests that both thumb prototypes will perform similarly at grasping and manipulation tasks. However, the rolling ellipsoidal joint introduces several key benefits for a small kinematic sacrifice: these include a magnetic restoring force from the ceramic ellipsoids, a spring restoring force from the flexure hinges, resistance to compressive loads, and lower vulnerability to catch points.

Finally, the comparison of the tendon-based MM with the standard joint-angle-based MM showed that both methods produce different results: while they are of similar magnitudes, the former showed relatively even manipulability, whereas the latter produced a key region of high manipulability. These results were comparable but not exact, as is predicted by their mathematical relationship: While most small local motions will map easily from joint angle space to tendon space, catch points still affect the tendon pathway's length in practice, causing performance to deviate from that predicted by any theoretical kinematic model. When operating the gimbal CMC joint prototype, the edges of the aluminum were observed to contact the moving tendons, leading to catch points and subsequent noise in the displacements of the tendons. If there is elasticity in the tendons, it was not significant enough to be measured as a contribution to any major discrepancies.

IX. CONCLUSION

We constructed a rolling ellipsoidal CMC joint on a robotic thumb with proportions similar to a human, with flexion–extension and abduction–adduction axes colocated. Due to the contact between the magnets, the compliant mechanism was capable of resisting high contact forces. The position and orientation of each link, along with the tendon excursions, were recorded as the thumb was moved throughout its workspace. We calculated and compared the standard MM and a tendon excursion-based metric. Two anthropomorphic thumb designs were studied: the gimbal CMC joint model and the biellipsoidal joint model. For each of these thumb designs, we analytically determined the forward kinematics from joint space to task space, and experimentally characterized the tendon-to-task space kinematics. Application of the MM to each model shows that the predicted region of highest manipulability within the thumb-tip's workspace is a well-defined region of the thumb's workspace. In both models, this region occurs just above the metacarpal phalanx of the fourth and fifth fingers, which is where the most common prehensile grasps require the highest manipulability. The shape of this region differs slightly between the two designs, with the biellipsoidal forward kinematics producing a more oblong result, but with a similar volume.

Either prototype is predicted to produce a similar performance in terms of manipulability, however, the biellipsoidal CMC joint has many practical advantages. First, it is able to better withstand the axial transmission of forces about the joint than an equivalent gimbal CMC joint, which would experience an equivalent loading as much higher shear forces on the crosssections of its

hinge joint pins. Second, a physical gimbal will always take up extra surrounding space to build, which limits the relative range of motion as compared with the biellipsoidal CMC joint. Finally, the ellipsoidal joint has better tendon management: for an equivalent range of adduction/abduction and flexion/extension motion, there are fewer inherent catch points in the biellipsoidal model, as the tendons can slide smoothly over the ellipsoidal surface when in contact.

Suggestions for future work include creating an analytical model for the forward kinematics of the tendon excursions and checking computationally for catch points in the model. This would allow us to analyze the tendon/joint space Jacobian at various poses analytically, elucidating further the relationships seen between the two models: this could determine whether the actual tendon behavior matches our models' assumptions. To do this, specific couplings between each joint angle and its neighboring tendon excursions must be determined: this is an arc-length calculation for hinge joints and a comparable calculation for the biellipsoidal joint.

ACKNOWLEDGMENT

The authors would like to thank Albert Okoh and Dipayan Das for their dedicated work on manufacturing small robotic parts for this research.

REFERENCES

- [1] H. Moravec, *Mind Children: The Future of Robot and Human Intelligence*. Cambridge, MA, USA: Harvard Univ. Press, 1988.
- [2] T. Zhang, W. Zhang, and M. M. Gupta, "An underactuated self-reconfigurable robot and the reconfiguration evolution," in *J. Mechanisms Mach. Theory*, vol. 124, pp. 248–258, 2018.
- [3] M. Martell, J. C. Diaz, and J. Schultz, "A linear multiport network approach for elastically coupled underactuated grippers," *J. Mechanisms Robot.*, vol. 9, no. 5, Oct. 2017, Art. no. 051012.
- [4] Y. Zhang, X. Xu, R. Xia, and H. Deng, "Stiffness-estimation-based grasping force fuzzy control for underactuated prosthetic hands," *IEEE/ASME Trans. Mechatron.*, vol. 28, no. 1, pp. 140–151, Feb. 2023.
- [5] F. Wang, Z. Qian, Y. Lin, and W. Zhang, "Design and rapid construction of a cost-effective virtual haptic device," *J. Trans. Mechatron.*, vol. 26, pp. 66–78, 2021.
- [6] S. Pulleyking, D. Das, and J. Schultz, "Simplified robotic thumb inspired by surgical intervention," in *Proc. IEEE 6th Int. Conf. Biomed. Robot. Biomechatronics*, 2016, pp. 1200–1206.
- [7] S. Pulleyking and J. Schultz, "Flexure hinge-based biomimetic thumb with a rolling-surface metacarpal joint," in *Proc. IEEE Int. Conf. Robot. Automat.*, 2020, pp. 2960–2966.
- [8] D. Das, N. Rake, and J. Schultz, "The TU hand: Using compliant connections to modulate grasping behavior," in *Proc. Robot. Grasping Manipulation Commun. Comput. Inf. Sci.*, 2018, pp. 57–83.
- [9] A. M. R. Agur and A. Dalley, *Grant's Atlas of Anatomy*. Philadelphia, PA, USA: Lippincott Williams and Wilkins, 2009.
- [10] J. Wang, Y. Wang, Y. Fei, and W. Chen, "Pneumatic bending soft actuator coupling with revolute joint with different boundary constraints," *IEEE/ASME Trans. Mechatron.*, vol. 28, no. 3, pp. 1245–1255, Jun. 2023.
- [11] A. M. Hollister, W. L. Buford, L. M. Myers, D. J. Giurintano, and A. Novick, "The axes of rotation of the thumb carpometacarpal joint," *J. Orthopaedic Res.*, vol. 10, no. 3, pp. 454–460, 1992.
- [12] A. Synek, M. Settles, and G. Stillfried, "Multi-body simulation of a human thumb joint by sliding surfaces," in *Proc. IEEE Robot. Automat. Lett. EMBS Int. Conf. Biomed. Robot. Biomechatronics*, 2012, pp. 379–384.
- [13] M. Andrychowicz et al., "Learning dexterous in-hand manipulation," *Int. J. Robot. Research*, vol. 39, no. 1, pp. 3–20, 2020.
- [14] A. Schmitz, U. Pattacini, F. Nori, L. Natale, G. Metta, and G. Sandini, "Design, realization and sensorization of the dexterous iCub hand," in *Proc. IEEE-RAS 10th Int. Conf. Humanoid Robots*, 2010, pp. 186–191.

- [15] D. H. Lee, J. H. Park, S. W. Park, M. H. Baeg, and J. H. Bae, "KITECH-Hand: A highly dexterous and modularized robotic hand," *IEEE/ASME Trans. Mechatron.*, vol. 22, no. 2, pp. 876–887, Apr. 2017.
- [16] H. Liu et al., "Multisensory five-finger dexterous hand: The DLR/HIT hand II," in *Proc. IEEE/RSJ Int. Conf. Intell. Robots Syst.*, 2008, pp. 3692–3697.
- [17] F. Ficuciello, A. Federico, V. Lippiello, and B. Siciliano, "Synergies evaluation of the SCHUNK S5FH for grasping control," in *Advances in Robot Kinematics*. Berlin, Germany: Springer, 2016, pp. 225–233.
- [18] J. T. Belter and A. M. Dollar, "Performance characteristics of anthropomorphic prosthetic hands," in *Proc. IEEE Int. Conf. Rehabil. Robot.*, 2011, pp. 1–7.
- [19] T. Yang, N. Sun, H. Chen, and Y. Fang, "Adaptive optimal motion control of uncertain underactuated mechatronic systems with actuator constraints," *IEEE/ASME Trans. Mechatron.*, vol. 28, no. 1, pp. 210–222, Feb. 2023.
- [20] W. Zhu et al., "A soft-rigid hybrid gripper with lateral compliance and dexterous in-hand manipulation," *IEEE/ASME Trans. Mechatron.*, vol. 28, no. 1, pp. 104–115, Feb. 2023.
- [21] L. Cao, A. T. Dolovich, A. L. Schwab, J. L. Herder, and W. Zhang, "Toward a unified design approach for both compliant mechanisms and rigid-body mechanisms: Module optimization," *J. Mech. Des.*, vol. 137, no. 12, Dec. 2015, Art. no. 122301.
- [22] T. Yoshikawa, "Manipulability and redundancy control of robotic mechanisms," in *Proc. IEEE Int. Conf. Robot. Automat.*, vol. 4, no. 2, pp. 3–9, Mar. 1985.
- [23] Y. Yokokohji, J. S. Martin, and M. Fujiwara, "Dynamic manipulability of multifingered grasping," *IEEE Trans. Robot.*, vol. 25, no. 4, pp. 947–954, Aug. 2009.
- [24] N. Xu, M. Dai, and X. Zhou, "Analysis and design of symmetric notch flexure hinges," *Adv. Mech. Eng.*, vol. 9, no. 11, pp. 1–12, 2017.
- [25] W. Chen et al., "Magnetic untethered peanutlike millirobot motion mode switching control," *IEEE/ASME Trans. Mechatron.*, vol. 28, no. 3, pp. 1638–1648, Jun. 2023.
- [26] E. M. Blake, "Upon the ruled surfaces generated by the plane movements whose centrodres are congruent conics tangent at homologous points," *Amer. J. Math.*, vol. 21, no. 3, pp. 257–69, 1899.
- [27] R. M. Murray, Z. Li, and S. Sastry, *A Mathematical Introduction to Robotic Manipulation*. Boca Raton, FL, USA: CRC Press, 2017.
- [28] M. Malhotra and Y. Matsuoka, "The relationship between actuator reduction and controllability for a robotic hand," in *Proc. IEEE 3rd RAS EMBS Int. Conf. Biomed. Robot. Biomechatronics*, 2010, pp. 331–336.
- [29] N. J. Rake, S. P. Skinner, G. D. O'Mahony, and J. A. Schultz, "Modeling and implementation of a simplified human tendon structure in a robotic finger," in *Proc. IEEE 6th Int. Conf. Biomed. Robot. Biomechatronics*, 2016, pp. 120–125.
- [30] J. Schultz and N. J. Rake, "A four-tendon robotic finger with tendon transmission inspired by the human extensor mechanism," *Bioinspiration Biomimetics*, vol. 16, no. 4, pp. 1–17, 2021.
- [31] T. Longtin Cohl, "Crosslink ellipse gears," Dec. 1, 2009. [Online]. Available: <https://www.thingiverse.com/thing:1367>
- [32] G. Glaeser, "Kinematics: Geometry in motion," in *Geometry and its Applications in Arts, Nature and Technology*, Berlin, Germany: Springer, 2020, pp. 415–458.
- [33] E. W. Weisstein, "Ellipse," *Wolfram MathWorld—A Wolfram Web Resource*, 2023.
- [34] Y. J. Kim, "Design of low inertia manipulator with high stiffness and strength using tension amplifying mechanisms," in *Proc. IEEE/RSJ Int. Conf. Intell. Robots Syst.*, 2015, pp. 5850–5856.
- [35] Y. J. Kim, J. I. Kim, and W. Jang, "Quaternion joint: Dexterous 3-DOF joint representing quaternion motion for high-speed safe interaction," in *Proc. IEEE/RSJ Int. Conf. Intell. Robots Syst.*, 2018, pp. 935–942.
- [36] S. Patel and T. Sobb, "Manipulator performance measures—a comprehensive literature survey," *J. Intell. Robotic Syst.*, vol. 77, pp. 547–570, 2015.
- [37] D. Pratichizzo, M. Pozzi, and M. Malvezzi, "Dexterous manipulation," in *Encyclopedia of Robotics*. Berlin, Germany: Springer, 2020.
- [38] H. Endo, "Examination of robotic manipulability indices to evaluate upper limb manipulability in digital human models," *Int. J. Hum. Factors Modelling Simul.*, vol. 6, no. 4, pp. 282–297, 2018.



Spenser Pulleyking (Graduate Student Member, IEEE) received the BSME degree in mechanical engineering from the University of Tulsa, Tulsa, OK, USA, in 2013, where he is currently working toward the Ph.D. degree in mechanical engineering.

His research interests include low-cost applications for robotic grasping, dexterous manipulation, and biomimetic soft/rigid hybrid robots.



Joshua Schultz (Senior Member, IEEE) received the BSME degree in mechanical engineering from Tufts University, Medford, MA, USA, in 2002, the M.S. degree in mechanical engineering from Vanderbilt University, Nashville, TN, USA, in 2004, and the Ph.D. degree in mechanical engineering from the Georgia Institute of Technology, Atlanta, GA, USA, in 2012.

He is an Associate Professor with the Department of Mechanical Engineering, University of Tulsa, Tulsa, OK, USA. His research interests include biologically inspired paradigms for robotic motion, including artificial muscles, soft robotics, and manipulation and grasping.

Dr. Schultz was named as an ARCS Scholar in 2011.